Capacitive sensing of test mass motion with nanometer precision over millimeter-wide sensing gaps for space-borne gravitational reference sensors

M. Armano *et al.* (LISA Pathfinder Collaboration)

Capacitive sensing of test mass motion with nanometer precision over millimeter-wide sensing gaps for space-borne gravitational reference sensors

M Armano,[1] H Audley,[2] G Auger,[3] J Baird,[4] M Bassan,[5] P Binetruy,[3, †] M Born,[2] D Bortoluzzi,[6] N Brandt,[7] M Caleno,[8] A Cavalleri,[9] A Cesarini,[10] A M Cruise,[11] K Danzmann,[2] R De Deus Silva,[1] R De Rosa,[12] L Di Fiore,[13] I Diepholz,[2] G Dixon,[11] R Dolesi,[10] N Dunbar,[14] L Ferraioli,[15, *] V Ferroni,[10] E D Fitzsimons,[16] R Flatscher,[7] M Freschi,[1] C García Marirrodriga,[8] R Gerndt,[7] L Gesa,[17] F Gibert,[10] D Giardini,[15] R Giusteri,[10] A Grado,[18] C Grimani,[19] J Grzymisch,[8] I Harrison,[20] G Heinzel,[2] M Hewitson,[2] D Hollington,[4] D Hoyland,[11] M Hueller,[10] H Inchauspé,[3] O Jennrich,[8] P Jetzer,[21] B Johlander,[8] N Karnesis,[2] B Kaune,[2] N Korsakova,[22] C J Killow,[22] J A Lobo,[17, †] I Lloro,[17] L Liu,[10] J P López-Zaragoza,[17] R Maarschalkerweerd,[20] D Mance,[15, ‡] V Martín,[17] L Martin-Polo,[1] J Martino,[3] F Martin-Porqueras,[1] S Madden,[8] I Mateos,[17] P W McNamara,[8] J Mendes,[20] L Mendes,[1] N Meshksar,[15] M Nofrarias,[17] S Paczkowski,[2] M Perreur-Lloyd,[22] A Petiteau,[3] P Pivato,[10] E Plagnol,[3] P Prat,[3] U Ragnit,[8] J Ramos-Castro,[23] J Reiche,[2] D I Robertson,[22] H Rozemeijer,[8] F Rivas,[17] G Russano,[10] P Sarra,[24] A Schleicher,[7] J Slutsky,[25] C F Sopuerta,[17] R Stanga,[26] T J Sumner,[4] D Texier,[1] J I Thorpe,[25] C Trenkel,[14] M Tröbs,[2] D Vetrugno,[10] S Vitale,[10] G Wanner,[2] H Ward,[22] P J Wass,[4] D Wealthy,[14] W J Weber,[10] L Wissel,[2] A Wittchen,[2] A Zambotti,[6] C Zanoni,[6] T Ziegler,[7] and P Zweifel[15]

(LISA Pathfinder Collaboration)

[1]*European Space Astronomy Centre, European Space Agency, Villanueva de la Cañada, 28692 Madrid, Spain*
[2]*Albert-Einstein-Institut, Max-Planck-Institut für Gravitationsphysik und Leibniz Universität Hannover, Callinstraße 38, 30167 Hannover, Germany*
[3]*APC, Univ Paris Diderot, CNRS/IN2P3, CEA/Irfu, Obs de Paris, Sorbonne Paris Cité, France*
[4]*High Energy Physics Group, Department of Physics, Imperial College London, Blackett Laboratory, Prince Consort Road, London, SW7 2BW, UK*
[5]*Dipartimento di Fisica, Università di Roma "Tor Vergata", and INFN, sezione Roma Tor Vergata, I-00133 Roma, Italy*
[6]*Department of Industrial Engineering, University of Trento, via Sommarive 9, 38123 Trento, and Trento Institute for Fundamental Physics and Application / INFN*
[7]*Airbus Defence and Space, Claude-Dornier-Strasse, 88090 Immenstaad, Germany*
[8]*European Space Technology Centre, European Space Agency, Keplerlaan 1, 2200 AG Noordwijk, The Netherlands*
[9]*Istituto di Fotonica e Nanotecnologie, CNR-Fondazione Bruno Kessler, I-38123 Povo, Trento, Italy*
[10]*Dipartimento di Fisica, Università di Trento and Trento Institute for Fundamental Physics and Application / INFN, 38123 Povo, Trento, Italy*
[11]*The School of Physics and Astronomy, University of Birmingham, Birmingham, UK*
[12]*Dipartimento di Fisica, Università di Napoli "Federico II" and INFN - Sezione di Napoli, I-80126, Napoli, Italy*
[13]*INFN - Sezione di Napoli, I-80126, Napoli, Italy*
[14]*Airbus Defence and Space, Gunnels Wood Road, Stevenage, Hertfordshire, SG1 2AS, UK*
[15]*Institut für Geophysik, ETH Zürich, Sonneggstrasse 5, CH-8092, Zürich, Switzerland*
[16]*The UK Astronomy Technology Centre, Royal Observatory, Edinburgh, Blackford Hill, Edinburgh, EH9 3HJ, UK*
[17]*Institut de Ciències de l'Espai (CSIC-IEEC), Campus UAB, Carrer de Can Magrans s/n, 08193 Cerdanyola del Vallès, Spain*
[18]*INAF Osservatorio Astronomico di Capodimonte, I-80131 Napoli, Italy and INFN sezione di Napoli, I-80126 Napoli, Italy*
[19]*DISPEA, Università di Urbino "Carlo Bo", Via S. Chiara, 27 61029 Urbino/INFN, Italy*
[20]*European Space Operations Centre, European Space Agency, 64293 Darmstadt, Germany*
[21]*Physik Institut, Universität Zürich, Winterthurerstrasse 190, CH-8057 Zürich, Switzerland*
[22]*SUPA, Institute for Gravitational Research, School of Physics and Astronomy, University of Glasgow, Glasgow, G12 8QQ, UK*
[23]*Department d'Enginyeria Electrònica, Universitat Politècnica de Catalunya, 08034 Barcelona, Spain*
[24]*CGS S.p.A, Compagnia Generale per lo Spazio, Via Gallarate, 150 - 20151 Milano, Italy*
[25]*Gravitational Astrophysics Lab, NASA Goddard Space Flight Center, 8800 Greenbelt Road, Greenbelt, MD 20771 USA*
[26]*Dipartimento di Fisica ed Astronomia, Università degli Studi di Firenze and INFN - Sezione di Firenze, I-50019 Firenze, Italy*

We report on the performance of the capacitive gap-sensing system of the Gravitational Reference Sensor (GRS) onboard the LISA Pathfinder (LPF) spacecraft. From in-flight measurements, the system has demonstrated a performance, down to 1 mHz, that is ranging between $0.7\,\mathrm{aF\,Hz^{-1/2}}$ and $1.8\,\mathrm{aF\,Hz^{-1/2}}$. That translates into a sensing noise of the test mass motion within $1.2\,\mathrm{nm\,Hz^{-1/2}}$ and $2.4\,\mathrm{nm\,Hz^{-1/2}}$ in displacement and within $83\,\mathrm{nrad\,Hz^{-1/2}}$ and $170\,\mathrm{nrad\,Hz^{-1/2}}$ in rotation. This matches the performance goals for LPF and it allows the successful implementation of the gravitational waves observatory LISA. A $1/f$ tail has been observed for frequencies below 1 mHz, the tail has been investigated in detail with dedicated in-flight measurements and a model is presented in the paper. A projection of such noise to frequencies below 0.1 mHz shows that an improvement of performance at those frequencies is desirable for the next generation of GRS sensors for space-borne gravitational waves observation.

I.   INTRODUCTION

Capacitive sensing is an established technique for the measurement of test mass (TM) motion in high precision space-borne experiments for the detection of gravitational waves [1–3], tests of the equivalent principle [4–6] and measurements of relativistic effects on precessing gyroscopes [7]. Capacitive sensing, often in combination with optical metrology [1–3], is used to provide the reference signals for the drag-free control system of a spacecraft [1–5, 7]. In this paper we report on the performance of the capacitive sensing system on board the LISA Pathfinder spacecraft.

LISA Pathfinder [1, 2, 8, 9] (LPF) is an European Space Agency mission dedicated to the demonstration of free-fall of a TM to the level required for the implementation of the future space-borne gravitational wave (GW) observatory, LISA [3] (Laser Interferometer Space Antenna). Moving to space is advantageous for a GW observatory as there is no seismic gravitational noise that limits the low frequency sensitivity of the ground based GW observatories. The free-falling TM, i.e., the reference for the geodesic motion, has to be protected from the external environmental disturbances, so it is placed within an electrode housing (EH) and a spacecraft. The spacecraft is then forced to follow the TM via micronewton thrusters and a drag-free control system. The core of the LPF and LISA instruments is then the Gravitational Reference Sensor (GRS) that incorporates the TM and its EH. The TM motion is sensed with a laser interferometer along a selected number of Degrees of Freedom (DoF) and along all DoFs by the GRS capacitive sensing system. The electrodes for the capacitive sensing are placed within the EH. The TM is composed of an Au-Pt alloy and effectively provides the other electrode for the capacitive sensing system. GRS capacitive sensing is a backup system for the optically controlled DoFs in case of a failure of the optical system [3]. Moreover the GRS capacitive sensing provides: i) an independent science readout of the TM position, which can be relevant especially at low frequency where structural deformation of the system can dominate the white readout noise; ii) an absolute reference for the TM position within the EH, both to center the TM to eliminate some sources of force and to allow calculation of forces from the TM-EH coupling.

The detection of gravitational waves in space requires that the stray forces perturbing the motion of a test mass be less than 3 and $12\,\mathrm{fm\,s^{-2}\,Hz^{-1/2}}$ at $1\,\mathrm{mHz}$ and $0.1\,\mathrm{mHz}$ respectively [3]. A symmetric design of the GRS has been selected for LPF in order to ensure stability down to $0.1\,\mathrm{mHz}$ and to avoid an excess of cross talk between non-science DoFs and the main science DoF [10, 11]. Moreover the TM is 'suspended' with no contact to the EH. This means that TM discharge is performed by UV lamp illumination [13] and that each TM is capacitively biased to a given voltage in order to allow for capacitive sensing of its motion. Since a number of physical effects perturbing the TM motion are inversely proportional to the gap between the TM and the EH [10–12], the LPF GRS has been designed to work with millimetre-wide sensing gaps, the widest sensing gaps ever implemented for a drag-free space mission [7, 14–16]. Biasing the TM results in a stiffness coupling, which allows the TM readout noise to leak into the TM acceleration noise. Increasing the gap to mm requires biasing of the TM with voltages of the order of one Volt. This sets a constraint on the readout noise of the sensing channels that are used to control the drag-free system of the spacecraft. Such sensing noise has to be limited to $\sim\mathrm{nm\ Hz^{-1/2}}$ in order to limit cross-talk into the GW sensing channels. In LPF this translates in a capacitive gap-sensing system with $\mathrm{aF\,Hz^{-1/2}}$ (equivalent to $\mathrm{nm\,Hz^{-1/2}}$) precision over a total capacitance of the order of pF (i.e., mm wide gaps).

The block diagram of the GRS capacitive sensing system on board LPF is reported in Fig. 1. We report one sensing channel for the x - ϕ DoF; the remaining channels are omitted for simplicity. The TM position sensing is based on measurement of the differential capacitance existing between electrodes and the TM along all DoFs. The TM motion causes an imbalance in capacitance on opposing sides of the TM, and thus an imbalance in AC currents flowing in primary windings of each differential transformer (sensing bridge). Two capacitive measurements are combined to calculate the TM displacement (x) and rotation (ϕ). Displacement is provided by the average of the two capacitive measurements while rotation is obtained by the difference. Similarly, the other 8 electrodes (not shown) are used to derive the remaining TM motion in y - θ and z - η DoFs. The TM is surrounded by four sensing / actuation electrodes per axis that are embedded and isolated inside the EH, with the EH being electrically grounded. For the purpose of sensing, a stable $100\,\mathrm{kHz}$ AC signal is applied via separate injection electrodes to the TM, i.e., by capacitive coupling

---

†Deceased
*Corresponding Author: luigi.ferraioli@erdw.ethz.ch
‡Corresponding Author: davor.mance@erdw.ethz.ch

between injection electrode, the TM and the EH. The amplitude of the injected signal is selected such as to produce a 0.6 V peak voltage on the TM [11]. It is useful to assign the sensing channels with specific names. In reference to Fig. 1, the electrode pair A+/A- defines a sensing channel that we call $1x$ while the electrode pair B+/B- defines the sensing channel $2x$. Analogously we have $1y$ and $2y$ sensing channels for the y - θ electrodes and $1z$ and $2z$ sensing channels for the z - η electrodes. This scheme is the same for both TMs (TM1 and TM2). More details on the electronics can be found in Appendix A.

In section II we report the measured performances of the GRS capacitive sensing system along all the LPF mission. In section III we perform an analysis of the noise components dominating at frequencies below 1 mHz. In section IV we discuss the outlook for the LISA GRS capacitive sensing system and in section V we draw our conclusions.

II. LONG TERM STUDY OF HIGH FREQUENCY SENSING NOISE

We performed an investigation of the GRS capacitive sensing noise at high frequencies over the period covering the LPF commissioning and science operations. The noise level has been calculated by taking the square root of the average power spectral density (PSD) in the frequency band [0.3, 0.5] Hz. In order to calculate the PSD we select non-overlapping time stretches of $N_s = 4000$ seconds for each noise run. For each segment we calculate the mean value of the PSD in the frequency band [0.3, 0.5] Hz. The value obtained is then averaged over all the available segments for the given noise run in order to provide the final average noise level for the corresponding run. Data are presented in Fig. 2 for all the sensing channels of the two LPF TMs. On Fig. 3 we present the relative change of the sensing noise level over the LPF mission with respect to the first measured value in Feb. 2016. The uncertainty reported in Fig. 2 is calculated as the ensemble standard deviation of the mean values for each noise run. For every TM there are two sensing channels per DoF (see Appendix A).

It can be immediately seen that all the sensing channels show a sensing noise below $1.8\,\mathrm{aF\,Hz}^{-1/2}$. As a consequence the sensing precision of the instrument is better than $2.4\,\mathrm{nm\,Hz}^{-1/2}$ in displacement and better than $170\,\mathrm{nrad\,Hz}^{-1/2}$ in rotation [†].

It is worth noting that the $1x$, $1y$, $1z$ channels performn systematically better than the $2x$, $2y$, $2z$ channels. Indeed, the $1x$, $1y$, $1z$ channels show a performance better than $0.8\,\mathrm{aF\,Hz}^{-1/2}$, which translates into a sensing precision for such channels better than $1.36\,\mathrm{nm\,Hz}^{-1/2}$ in displacement and better than $118\,\mathrm{nrad\,Hz}^{-1/2}$ in rotation. Such values are as good as the calculated thermal noise limit for the instrument (see Appendix B).

The difference between the $1x$, $1y$, $1z$ and the $2x$, $2y$, $2z$ channels is not completely understood. In principle there is no difference between the electronics of the different channels. Random oscillations of the performance connected to differences between electronic components is excluded because the $2x$, $2y$, $2z$ channels are systematically worse than the $1x$, $1y$, $1z$ channels. Moreover we observed larger variability of the $2x$, $2y$, $2z$ channels, which is consistent with their noise coming from non-intrinsic pickup. The origin of such difference is more likely to be searched in the integration process of the different boards as the mounting position of the $2x$, $2y$, $2z$ boards is different from the position of the $1x$, $1y$, $1z$ boards. Dedicated investigations of this issue will be performed for the design of the LISA GRS hardware.

An excess of noise for two measurements performed on Apr. 2017 is noted in Fig. 2. There are indications that the origin of such excess is connected with an excess of electromagnetic disturbance due to non-nominal activity on-board the spacecraft. As a consequence such data points are not representative of the instrument performance and are reported only for completeness.

In Fig. 3, the relative variation of the sensing noise is reported for different measurements over the LPF mission duration. It is clearly observed that the sensing noise has been stable within 10% of the first measured value in Feb 2016. The only exception is channel TM2 $2y$, which exhibits a reduction of performance of 15% since the beginning of the mission.

[†] Two readout channels are combined to obtain displacement and rotation. Displacement is provided by the average of the two capacitive measurements while rotation is obtained by the difference.

III.   SENSING NOISE PERFORMANCE BELOW 1 mHz

A.   Noise Measurements

GRS sensing noise can be measured on the full frequency band only with the TM held in place near the nominal geometric center of the EH by the dedicated Grabbing Positioning Release Mechanism (GPRM) used to transition the TM to and from the free-fall condition [17]. In normal operating conditions, thruster noise is dominating over GRS sensing noise above 3 mHz, while noise from the spacecraft dominates the GRS sensing noise for frequencies below 1 mHz. When grabbed, the TMs are biased through the direct contact provided by the plungers (metal fingers). As the TMs cannot move, the drag free control scheme is not active during the measurement. Having grabbed TMs is advantageous for the measurement of the GRS sensing noise as the spacecraft dynamics is highly suppressed thanks to the rigid contact of the TM and the spacecraft by the plungers. Nevertheless, we cannot exclude that some extra noise enters the measurement because of the contact between TM and plungers (e.g., thermal fluctuation of plungers' length resulting in TM motion). GRS sensing noise with grabbed TMs has been measured three times. The first two measurements were performed during LPF commissioning in Feb. 2016. The third measurement was performed during the LPF de-orbiting maneuvers in Apr. 2017. Fig. 4 reports the GRS sensing time series acquired during LPF commissioning in Feb. 2016.

B.   Analysis of Data

We performed a fit to the noise PSD for the different sensing channels in order to identify a noise model that works both at low and high frequency. The selected model includes two low frequency contribution with $1/f$ shape and one flat high frequency contribution. Such a model has been designed on the basis of physical considerations of the possible noise sources (see Appendix B). The model for the GRS capacitive sensing noise is:

$$\mathrm{PSD}_{ij} \left[\frac{\mathrm{aF}^2}{\mathrm{Hz}} \right] = \mathrm{A}_{ij}^2 + \left(\mathrm{B}\,\Delta_{ij}\,10^{-6} \right)^2 \left(\frac{10^{-3}\ \mathrm{Hz}}{f} \right) + \mathrm{C}_j^2 \left(\frac{10^{-3}\ \mathrm{Hz}}{f} \right). \tag{1}$$

Here, i is the index of a given measurement while j is an index identifying the given sensing channel. A_{ij} aF Hz$^{-1/2}$ is the level of the high frequency white noise for the measurement i and the channel j. B ppm Hz$^{-1/2}$ is the coefficient of the $1/f$ TM bias instability noise that is multiplicative with the test mass displacement Δ_{ij}. Here ppm refers to part-per-million. TM bias voltage is common to both TMs and it is applied to TMs from the injection electrodes that are not used for sensing. It is, therefore, a noise term in common to all the sensing channels. C_j aF Hz$^{-1/2}$ is the coefficient of a $1/f$ component of the noise depending on the performance of the single channel electronics. Therefore we expect a different C_j for each channel j. It is worth noting that we can expect some variability of the C_j coefficients with different measurements. In particular we can expect changes in the C_j noise term between the measurements performed on Feb. 2016 and on Apr. 2017, due to the amount of time separating the two measurements. As the majority of the channels do not show clear evidence for a worsening of the low frequency performance over the mission duration, we decided to apply the same C_j for fitting the three available datasets. Such a choice allowed us to keep the number of parameters for the low frequency fit to 13 (B plus C_j with $j = 1, \ldots, 12$) compared to the 37 (B plus C_{ij} with $i = 1, \ldots, 3$ and $j = 1, \ldots, 12$) required if we would allow for a full variability of the C_j coefficients. It is worth noting that the noise term modelled by B is TM position dependent, therefore it manifests itself only when the TM is displaced from its center position within the EH. On the other hand, the noise term modelled by C is present independently of the TM displacement and indicates the onset of a low frequency noise tail even when the TM is centered within the EH.

The high frequency noise contribution ($f \geq 1\,\mathrm{mHz}$) is expected to be independent from the low frequency noise terms (see Appendix B). Therefore the A_{ij} terms have been identified independently from the B and C_j terms, and for each measurement, with a maximum likelihood parameter estimation procedure on the high frequency part of the spectrum ($f \geq 20\,\mathrm{mHz}$). The B and C_j coefficients, on the other hand, were estimated using a global parameter estimation method, which included all the available measurements for all the channels at the same time. A Markov Chain Monte Carlo (MCMC) method [18–20] was used as the parameter estimation technique. MCMC methods are advantageous over other techniques as they are straightforward to implement and allow the estimation for the mean value of the parameters and their posterior distribution.

The coefficients derived by the parameter identification procedure provide the amplitude of the corresponding noise term at 1 mHz. The limit of 1 mHz was selected as it is the lowest frequency boundary of the LPF noise requirement. The model assumes that the three contributions add up incoherently to provide the final sensing noise. Results of the

MCMC parameter estimation are reported in Tab. I. We report the average of the MCMC chains as an estimate of the parameter values and their standard deviations as an estimate of their error. As reported in Tab. I we obtained a value of B $= 31 \pm 2\,\mathrm{ppm\,Hz^{-1/2}}$ at 1 mHz, which translates into B $\approx 100\,\mathrm{ppm\,Hz^{-1/2}}$ at 0.1 mHz. B represents the magnitude of the noise coming from the TM bias voltage instability. It has been estimated to be $\sim 50\,\mathrm{ppm\,Hz^{-1/2}}$ at 1 mHz during the on-ground test campaigns. Ground measurements were performed with TM simulators, which provided a differential capacitance for simulating TM displacement. The stability of the simulators affects the final result of the measurement. As a matter of fact, the grabbed TM measurement during flight operations proved to be more stable than the TM simulators used for on-ground measurements during test campaigns.

In Fig. 5 we report the square root of the PSD for three selected channels. Together with data, we report the corresponding models provided by equation (1) with the parameters reported in Tab. I. The PSD was calculated with Welch's averaged periodogram method [22]. Data were cut into overlapping segments of 4×10^4 seconds and windowed with a minimum 4-sample BlackmanHarris window [23]. All data were processed with LTPDA [24, 25]. The lowest four data bins were discarded as they are affected by a systematic bias due to the window spectral leakage. Such a procedure allows for the PSD estimation down to 0.1 mHz. The chosen data segment length allowed 6 and 10 periodogram averages for the measurements performed in Feb. 2016 and Apr. 2017 respectively.

In Fig. 5C, it is worth noting that the difference in the $1/f$ tail below 1 mHz for Feb. 2016 and Apr. 2017 is entirely induced by the difference in the z position of TM1 during the two experiments. During the Feb. 2016 measurements, the differential capacitive readout for the TM1 $1z$ channel was -3.4 fF, which corresponds to an equivalent off-center displacement of TM1 along negative z of $\sim 5.8\,\mu$m. On the other hand, the same readout channel during the Apr. 2017 measurement was reporting -21.3 fF, which corresponds to an equivalent off-center displacement along negative z of $\sim 36\,\mu$m. Larger TM displacement is proportional to an increase of the contribution of the B noise term in equation 1. As can be seen in Fig. 5C, the model in equation 1, with the parameters in Tab. I, correctly describes the increase of the position dependent noise term during Apr. 2017.

It is observed in Tab. I that the value of the C coefficient for channels $2x$, $2y$, $2z$ is often larger than the C value for the corresponding $1x$, $1y$, $1z$ channels. The analysis of the coherence between the $2x$, $2y$, $2z$ channels shows a significative degree of coherence between channel $2y$ and channels $2x$ and $2z$ respectively. Such coherence is clearly measurable at high frequency and it extends to low frequency barely unchanged. This observation indicates that the same mechanism affecting high frequency noise is extending to low frequency as well and it results in an excess of low frequency noise for the $2x$, $2y$, $2z$ channels, compared to $1x$, $1y$, $1z$ channels.

IV. IMPLICATIONS FOR LISA

In LISA [3] the attitude of one spacecraft is controlled on the position of the other two in order to keep the constellation aligned. The main science DoFs are controlled by optical readout while the other DoFs are controlled by GRS capacitive sensing readout. GRS capacitive sensing provides redundancy for the main science DoFs, while some command schemes could solely use GRS capacitive sensing for special purposes. The LISA spacecraft and constellation control do not necessarily require an improvement of the high frequency GRS capacitive sensing performance with respect to the ones already demonstrated by LPF. On the other hand, the science objectives of LISA would benefit from more stringent constraints on the low frequency part of the GRS sensing performances. In order to deliver the required science performance in LISA, the GRS sensing is required to provide a performance at the level of $5\,\mathrm{nm\,Hz^{-1/2}}$ over the whole LISA measurement band [3]. While the requirements are defined for the frequency band $0.1\,\mathrm{mHz} \leq f \leq 0.1\,\mathrm{Hz}$, the science goal is defined on an extended band of $20\,\mu\mathrm{Hz} \leq f \leq 1\,\mathrm{Hz}$. The level of $5\,\mathrm{nm\,Hz^{-1/2}}$ is easily satisfied if we set a sensing goal to the same level of LPF, i.e., $1\,\mathrm{aF\,Hz^{-1/2}}$. LPF measurements have already demonstrated the capability of the GRS to reach such a level for frequencies $\geq 1\,\mathrm{mHz}$.

Using the model developed for LPF in equation 1, with the parameters estimated from LPF data in Tab. I, we have projected the expected contribution of the LPF GRS capacitive sensing noise to the LISA measurement band in Fig. 6. The contribution from position dependent noise has been calculated for three different TM displacement from the central position, $1\,\mu$m, $10\,\mu$m and $100\,\mu$m respectively. As can be seen, noise of type C (position independent) dominates the current low frequency noise budget for a centered TM. Only if the TM off-center displacement is grater than $10\,\mu$m the B and C contributions are comparable. B starts dominating the noise budget only for sensibly off-centered TM.

Fig. 6 clearly indicates that an improvement of the low frequency performance is desirable for the LISA GRS capacitive sensing system. Since the two noise contributions (B and C) have different origin, their improvement requires different strategies. Position dependent noise originates from the instability of the TM voltage bias (see Appendix B). A strategy for an improvement of such noise contribution has been already investigated in a prototype of the LISA GRS sensing electronics [26]. A strategy for the mitigation of the position independent noise (C) will be

investigated for the design of the next iteration of the LISA GRS sensing electronics. It is highly likely that such noise originates in the last stages of the sensing circuit. The main candidates for this are the demodulator circuit and the ADC (see Appendix B). It is worth noting that the position independent noise (C) can be affected by additional noise coming from the contact of the TM with the plungers. Such terms should therefore be considered as upper limits to the GRS sensing performance.

V. CONCLUSIONS

We have presented the in-flight LISA Pathfinder performance of the GRS capacitive sensing system. We have observed that all the readout channels show a sensing noise below $1.8\,\mathrm{aF\,Hz^{-1/2}}$ for frequencies larger than $1\,\mathrm{mHz}$, equivalent to a TM displacement noise of $2.4\,\mathrm{nm\,Hz^{-1/2}}$. Half of the sensing channels ($1x$, $1y$, $1z$ on both TMs) have demonstrated a sensing noise below $0.8\,\mathrm{aF\,Hz^{-1/2}}$, which corresponds to the limit due to thermal noise in the circuit elements. The GRS sensing noise was monitored during LPF noise runs from Feb. 2016 to May 2017. Data show that all the sensing channels were stable within 10% of the first measured value.

GRS sensing noise at frequencies below $1\,\mathrm{mHz}$ was measured during the LPF commissioning phase in Feb. 2016 and during the LPF de-orbiting maneuvers in Apr. 2017 with grabbed TMs. The observed sensing noise has a PSD which is flat from the highest reachable frequency down to $1\,\mathrm{mHz}$. Below $1\,\mathrm{mHz}$ we observe a rising tail showing a $1/f$ behaviour in power. A model for the low frequency noise has been developed based on physical considerations for the origin of the different contributions. The parameters of the model were estimated from the analysis of the available data. The noise model contains two independent terms contributing to the low frequency tail. One is common for all the sensing channels and it depends from the TM off-center position within its electrode housing. The other depends on the particular sensing channel. The source of the TM position dependent noise is the instability of the TM voltage biasing that couples with TM displacement. Channel dependent noise originates in the last stages of the sensing circuits (demodulator and/or analog to digital converter). It is worth noting that the in-flight measurement of the position dependent noise shows a value of $31\,\mathrm{ppm\,Hz^{-1/2}}$ at $1\,\mathrm{mHz}$ compared with an expected value of $50\,\mathrm{ppm\,Hz^{-1/2}}$.

The implications of the present results for the future gravitational waves observatories (LISA) have been analyzed. The LPF GRS sensing performance at $f \geq 1\,\mathrm{mHz}$ satisfies the requirements for the implementations of the science objectives of LISA even though an improvement of the low frequency ($f < 1\,\mathrm{mHz}$) performance would be desirable. While a strategy for the mitigation of the TM position dependent noise is already under investigation, mitigating the position independent noise will require careful design of future iterations of the LISA GRS electronics.

Appendix A: LISA Pathfinder GRS Sensing Electronics

GRS sensing electronics (SE) provides position measurements of the GRS reference TM for all DoFs [10]. This is needed for precise drag-free spacecraft control on those axes not controlled by the optical metrology. In addition, the GRS SE can actuate the TM using electrostatic forces, which is used to keep the TM centered in its enclosure or to follow a certain guidance. We refer to Fig. 1 for a simplified block-diagram of one sensing channel of LPF GRS SE. Two identical sensing channels are used for each axis, i.e. six channels altogether per TM. TM position-sensing is based on measurement of the differential capacitance between the electrodes and TM along all DoFs. TM motion causes an imbalance in capacitance on opposing sides of TM, and thus an imbalance in AC currents flowing in the primary windings of each differential transformer (sensing bridge). Each primary current is terminated to ground via the actuation capacitor C_A, which also serves as a filter for the actuation voltage and provides a low-impedance path to ground for the sensing bridge operating at $100\,\mathrm{kHz}$. Both sensing and actuation can operate simultaneously as C_A does not provide a low-impedance path to ground for the actuation signals at audio frequencies (60-270 Hz).

The Trans-Impedance Amplifier (TIA) converts the current flowing in the transformer secondary winding into an AC voltage at $100\,\mathrm{kHz}$ that is further amplified by the main amplifier. The amplitude of this voltage follows the variation of the nominal gap between TM and the electrode housing where nominal gap is $4\,\mathrm{mm}$ for x-axis. A gain switching is implemented for the main amplifier: high gain for small TM displacement $\pm 0.12\,\mathrm{pF}$ ($\pm 200\,\mu\mathrm{m}$) science operations, i.e. High Resolution (HR) mode and low gain for large TM displacement $\pm 2.5\,\mathrm{pF}$ ($\pm 2.5\,\mathrm{mm}$) non-science operations, i.e. Wide Range (WR) mode.

The transformer bridge is an AC coupled circuit, with the transformer core and winding optimized for $100\,\mathrm{kHz}$ operation. In order to improve Signal-to-Noise Ratio (SNR) the bridge operates at resonance, for which the parallel capacitors C_P are tuned with the inductance L of the primary windings to operate the bridge at $100\,\mathrm{kHz}$, thus achieving a minimum sensing noise at this frequency. The decoupling capacitors, C_D, and resistors, R_{FB}, in the TIA feedback attenuate DC and low-frequency components originating from actuation. The main amplifier, G, is also AC

coupled. This is particularly important in the WR mode when actuation voltages are large (130 V), thus protecting the amplifier from saturation. A narrow, band-pass filter is implemented after the main amplifier, consisting of second order High-Pass (HP) and Low-Pass (LP) filters. It is used to isolate only the frequencies around 100 kHz. The modulation of the amplitude of the AC signal represents the TM motion. Its amplitude is extracted by a standard synchronous demodulation technique. A properly phased 100 kHz signal is used to control switches that make an AC signal inversion and thus generate a fully rectified signal. The rectified signal is then LP filtered in the sensing frequency band ($f < 10$ Hz) and finally digitized by an Analog to Digital Converter (ADC). The ADC has its own voltage reference that is different from the reference used to generate the stable 100 kHz injection bias.

Appendix B: Sensing Noise Sources

The sensitivity, i.e. the SNR, of the sensing circuit depends on the level of the injection bias and the circuit noise. The injection bias amplitude affects directly the sensing gain. Since in the GRS this amplitude is kept low to prevent back-action forces on TM [11], the sensing noise must be reduced as much as possible. The sensitivity of the capacitive measurement is limited by the performance (the noise) of the front stage, i.e. of the transformer bridge and the pre-amplifier (TIA). The quality factor Q of the differential transformer is inversely proportional to the transformer losses. These losses produce thermal noise, which is the dominant noise source in the circuit [21]. The square root of the PSD (ASD) of the differential capacitance noise caused by the bridge thermal noise is expressed by the equation (B1):

$$S_{\Delta C-\mathrm{BR-th}}^{1/2} = \frac{1}{V_{\mathrm{TM}}} \sqrt{\frac{8k_B T}{\omega_0^3 LQ}}. \tag{B1}$$

Where V_{TM} is the amplitude of the injection bias applied to TM, k_B is the Boltzmann constant, T is the absolute temperature and ω_0 is resonant angular frequency of the bridge. The frequency, inductance and quality factor cannot be made arbitrarily large since increasing one parameter reduces the other in a practical transformer design. For $V_{\mathrm{TM}} = 0.6$ V, $T = 300$ K, $\omega_0 = 2\pi f_0$, $f_0 = 100$ kHz, $L = 4.2$ mH and $Q = 150$, as in LPF GRS SE, the ASD of the expected capacitance noise is 0.78 aF Hz$^{-1/2}$. This design complies with the required sensitivity of 1 aF Hz$^{-1/2}$, which is equivalent to the displacement sensitivity of 1.7 nm Hz$^{-1/2}$.

The TIA gain fluctuation and amplifier noise are the second most important noise sources of the front-end stage. With the implemented design, the TIA output depends on only a few parameters [21] as shown by equation (B2):

$$V_{\mathrm{TIA}} = K \frac{C_A}{C_A + C_P} \frac{2\Delta C}{C_{\mathrm{FB}}} V_{\mathrm{TM}}. \tag{B2}$$

Where K is the transformer coupling factor between the primary and secondary windings, C_A and C_P are actuation and resonance (parallel) tuning capacitors, ΔC is differential capacitance measuring the TM displacement and rotation, C_{FB} is the TIA feedback (gain) capacitor and V_{TM} is the TM injection bias amplitude. Factor 2 in equation (B2) comes from the differential measurement, i.e. the use of two TIAs in the front-end. Since C_P is much smaller than C_A ($C_P \sim 3\% \, C_A$) and $K > 0.9$, the first factor in equation B2 is almost 1. The capacitance C_P consists of the lumped capacitance of the electronics and the capacitance of the cable that connects the electronics with the TM electrodes, both assumed to be stable. Small C_P fluctuations are further attenuated by the larger C_A value in the $C_A + C_P$ term in equation B2. As a consequence, any fluctuation of the capacitance C_A is effectively attenuated by the term $C_A/(C_A + C_P)$ in equation B2. The planar transformer design, using a Printed Circuit Board (PCB) with implanted windings as PCB tracks and a glued stack of primary and secondary windings, ensures stable coupling K and stable inter- and intra-winding stray capacitances. Therefore, the sensing gain will depend predominantly on the stability of the injection bias amplitude V_{TM} and on the stability of the TIA feedback capacitor C_{FB}, the latter located in each arm of the secondary winding (see Fig. 1). Any instability in the injection bias amplitude translates in a gain fluctuation and mimics TM motion causing low frequency noise proportional to the TM out-of-center position (ΔC).

C_{FB} are stable NPO-type ceramic capacitors with a capacitance of 3.3 pF. Their temperature sensitivity of 30 ppm/K does not affect the sensing gain at 1 mHz as long as the electronics temperature noise is less than ~ 3 K Hz$^{-1/2}$. During LPF noise runs in space, the temperature instability of the GRS SE PCBs was < 0.1 K Hz$^{-1/2}$ at 1 mHz. This temperature noise corresponds to a gain instability of 30 ppm K^{-1} × 0.1 K Hz$^{-1/2}$ = 3 ppm Hz$^{-1/2}$, which is more than 10 times smaller than the instability of the injection bias.

The TIA noise is dominated by the amplifier current noise flowing through the feedback impedance consisting of the C_{FB} capacitor and a large 5.6 MΩ parallel resistor R_{FB}, the latter is used to limit the DC gain and thus prevent

saturation effects. In the GRS SE a combination of a discrete transistor stage and an integrated circuit amplifier is implemented for the TIA to lower both the voltage and current noise and ensure low input capacitance.

The narrow band-pass filter that follows the sensing front stage can itself cause gain instability when the temperature fluctuates. The same type of ceramic capacitors are used to set HP and LP filter corner-frequencies. A capacitance shift caused by temperature fluctuation can change the gain at the center frequency (100 kHz) and thus cause low-frequency noise. The DC performance of the filter is not important since the filter operates in the AC domain. With the level of temperature noise measured in space, the temperature effects can only be visible below 1 mHz.

The demodulator, consisting of an analog switch and the DC amplifier-filter, is very important for the DC performance of the sensing circuit. Nonlinearity in the switching (switch charge injection effects) and crosstalk from the digital switching control circuit to analog circuit can increase the white noise level. The large temperature sensitivity of the analog switch series resistance, which would show up as a low-frequency noise, is handled by signal buffering. On the other hand, the buffer-amplifier low-frequency noise cannot be removed.

The $1/f$ noise of the last sensing circuit stage, which includes the LP filter noise and the ADC noise originating in its internal front circuit, can be attenuated in the 1 mHz band by proper gain distribution in the whole sensing circuit. This requires that most of the gain is set on the TIA and the main amplifier. The 16-bit ADC quantization noise would be the dominating noise source in the noise budget if the HR - WR gain switching, discussed in previous section, had not been implemented.

Acknowledgments

[1] M. Armano, et al., Sub-Femto-g Free Fall for Space-Based Gravitational Wave Observatories: LISA Pathfinder Results. Physical Review Letters, **116**(23), 1-10 (2016).
[2] M. Armano et al., LISA Pathfinder: First step to observing gravitational waves from space. Journal of Physics: Conference Series, **840**, 012001 (2017).
[3] K. Danzman et. al., LISA Laser Interferometer Space Antenna, A proposal in response to the ESA call for L3 mission concepts (2016).
[4] J. Bergé, P. Touboul and M. Rodrigues, Status of MICROSCOPE, a mission to test the Equivalence Principle in space, Journal of Physics: Conference Series **610**, 012009 (2015).
[5] J. Bergé, P. Touboul, M. Rodrigues and F. Liorzou, MICROSCOPE: five months after launch, Journal of Physics: Conference Series **840**, 012028 (2017).
[6] T. J. Sumner, J. Anderson, J.-P. Blaser, et al., STEP (satellite test of the equivalence principle), Advances in Space Research, **39**, 254-258 (2007).
[7] S. Buchman and J. P. Turneaure, The effects of patch-potentials on the gravity probe B gyoscopes. Review of Scientific Instruments **82**(7), 074502 (2011).
[8] F. Antonucci et al., From laboratory experiments to LISA Pathfinder: achieving LISA geodesic motion, Class. Quantum Grav. **28**, 094002 (2011).
[9] F. Antonucci et al., LISA Pathfinder: mission and status, Class. Quantum Grav. **28**, 094001 (2011).
[10] W. J. Weber et al., Position sensors for flight testing of LISA drag-free control, SPIE Proc. 4856, 31 (2002).

[11] R. Dolesi at al., Gravitational sensor for LISA and its technology demonstration mission, Class. Quantum Grav. 20 S99-S108 (2003).

[12] A. Cavalleri, G. Ciani, R. Dolesi, A. Heptonstall, M. Hueller, D. Nicolodi, S. Rowan, D. Tombolato, S. Vitale, P. J. Wass and W. J. Weber, Increased Brownian Force Noise from Molecular Impacts in a Constrained Volume, Phys. Rev. Lett. **103**, 140601 (2009).

[13] M. Armano, H. Audley, G. Auger, et al., Charge-Induced Force Noise on Free-Falling Test Masses: Results from LISA Pathfinder. Physical Review Letters **118**, 171101 (2017).

[14] P Touboul, G Métris, V Lebat and A Robert, The MICROSCOPE experiment, ready for the in-orbit test of the equivalence principle, Class. Quantum Grav. **29**, 184010 (2012).

[15] R. Floberghagen, M. Fehringer, D. Lamarre, et al., Mission design, operation and exploitation of the gravity field and steady-state ocean circulation explorer mission, J Geod, **85**, 749 (2011).

[16] E Davis, et al., The GRACE mission: meeting the technical challenges, 50th International Astronautical Congress, IAF-99-B.2.05 Conference (1999) AAS 90-034.

[17] C Zanoni, D Bortoluzzi, J W Conklin, I Köker, B Seutchat, S Vitale, Summary of the results of the LISA-Pathfinder Test Mass release, Journal of Physics: Conference Series **610**, 012022 (2015).

[18] L. Ferraioli et. al., Improving Bayesian analysis for LISA Pathfinder using an efficient Markov Chain Monte Carlo method, Exp. Astron. **37**, 109 (2014).

[19] N. Karnesis et. al., Bayesian model selection for LISA pathfinder, Phys. Rev. D **89**, 062001 (2014).

[20] M. Nofrarias, C. Röver, M. Hewitson, A. Monsky, G. Heinzel, K. Danzmann, L. Ferraioli, M. Hueller, S. Vitale, Bayesian parameter estimation in the second LISA Pathfinder mock data challenge, Phys. Rev. D **82**(12), 122002 (2010).

[21] D. Mance, Development of electronic system for sensing and actuation of test mass of the inertial sensor LISA, PhD Thesis University of Split (2012).

[22] P. D. Welch, The Use of Fast Fourier Transform for the Estimation of Power Spectra: A Method Based on Time Averaging Over Short, Modified Periodograms, IEEE Transactions On Audio and Electroacustics **AU-15**, 70 (1967).

[23] F. J. Harris, On the use of windows for harmonic analysis with the discrete Fourier transform, Proc. IEEE **66**, 51 (1978).

[24] M. Hewitson et al., Data analysis for the LISA Technology Package, Class. Quantum Grav. **26**, 094003 (2009).

[25] F. Antonucci et al., LISA Pathfinder data analysis, Class. Quantum Grav. **28**, 094006 (2011).

[26] D. Mance, P. Zweifel, L. Ferraioli, J. ten Pierick, N. Meshksar and D. Giardini, GRS electronics for a space-borne gravitational wave observatory, Journal of Physics: Conference Series **840**, 012040 (2017).
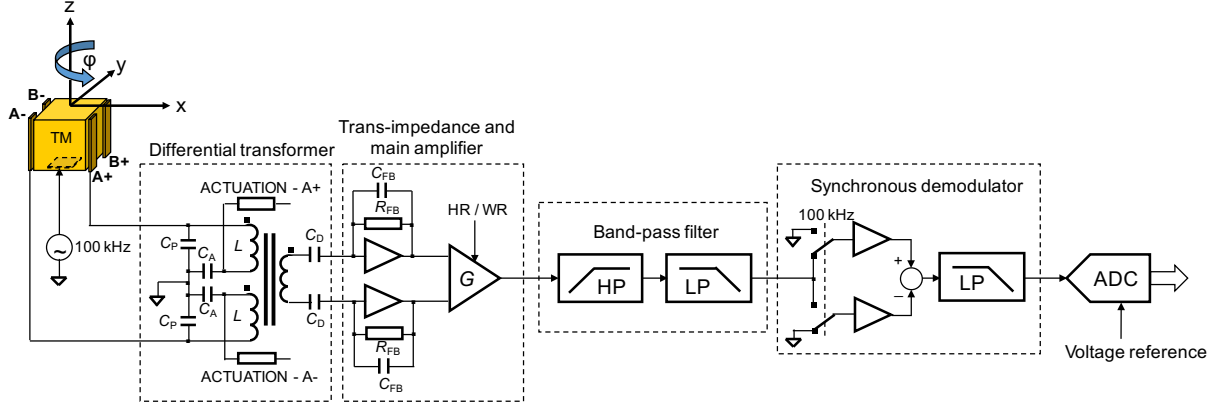
Figures

FIG. 1: A block diagram of the single TM sensing channel electronics along the x axis. Two pairs of electrodes (A+/A-, B+/B-) allow simultaneous measurement of the TM displacement and rotation, which is achieved by measurement of the gaps between the TM and the electrodes at opposing sides of the TM. For small TM displacements, the capacitance is proportional to the respective TM - electrode gap. The actuation circuit (one for each electrode) electrostatically applies forces and torques on the TM using the same electrodes. An AC injection bias (100 kHz) is injected on the TM. Differential currents are measured, amplified and converted into an AC sensing voltage proportional to the TM motion. Sensing voltage is filtered at the AC injection frequency, and its amplitude is demodulated and finally converted into a digital value.
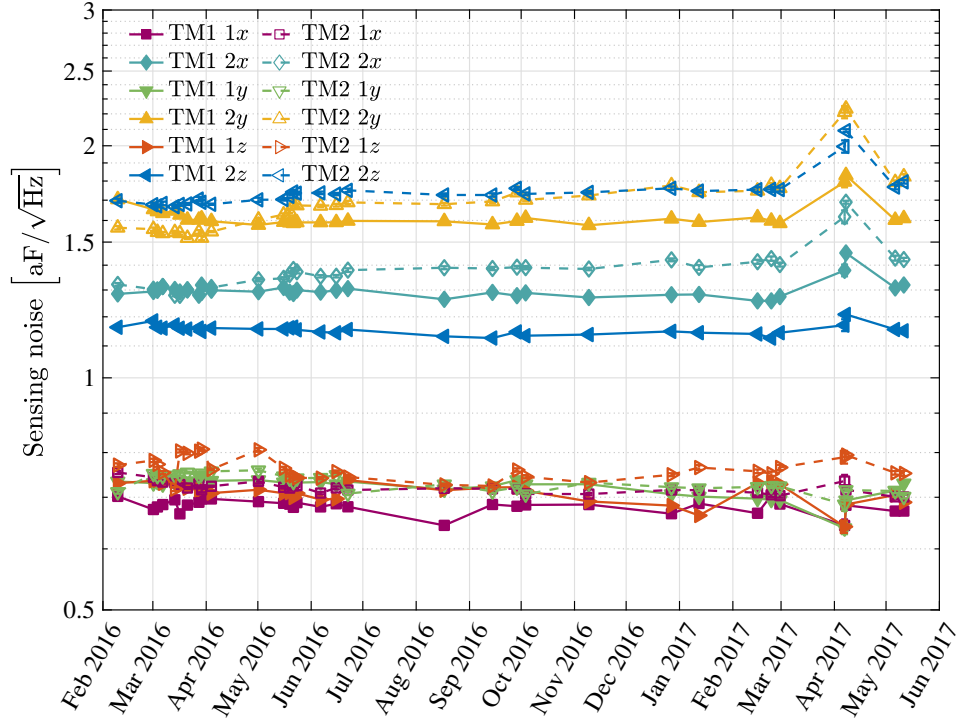
FIG. 2: Average square root of PSD of the GRS capacitive sensing channels measured during the LPF mission. As the data sample rate is $1\,\mathrm{Hz}$ and the sensing noise is flat down to 1 mHz, the values presented are representative of the precision of the instrument in the frequency range $[10^{-3},\,0.5]\,\mathrm{Hz}$. Sensing precision is reported in $\mathrm{aF\,Hz^{-1/2}}$ as this is the physical observable sensed by the instrument (differential capacitance). In order to convert such values in $\mathrm{nm\,Hz^{-1/2}}$ the conversion factor $1.7\,\mathrm{nm/aF}$ applies.
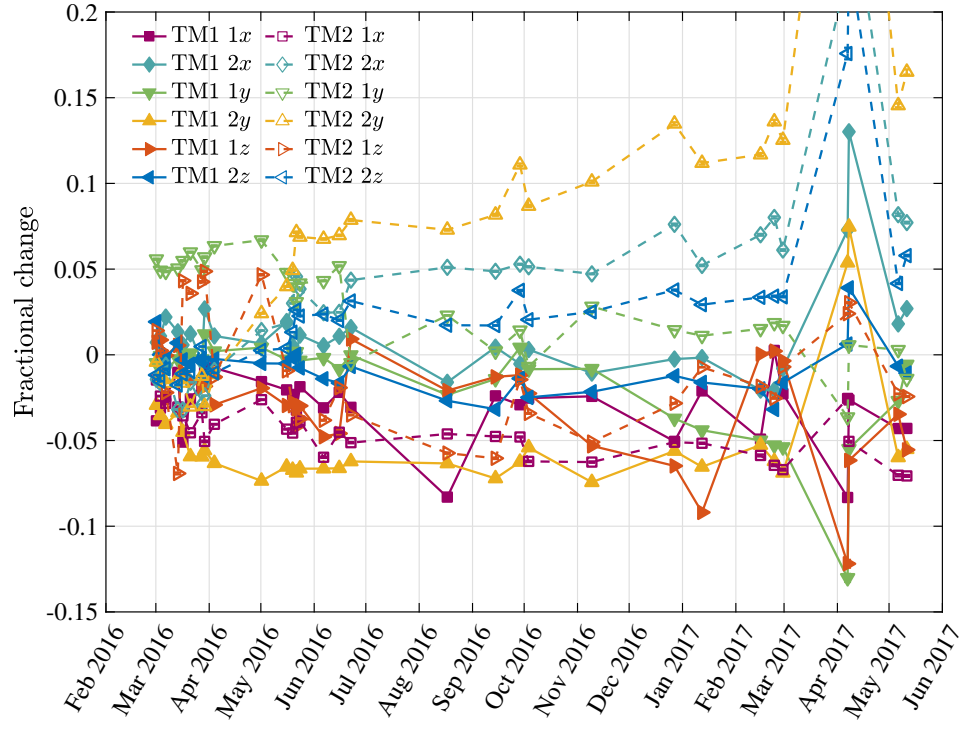
FIG. 3: Fractional change of the average sensing noise with respect to the first in-flight measurement performed in Feb 2016.
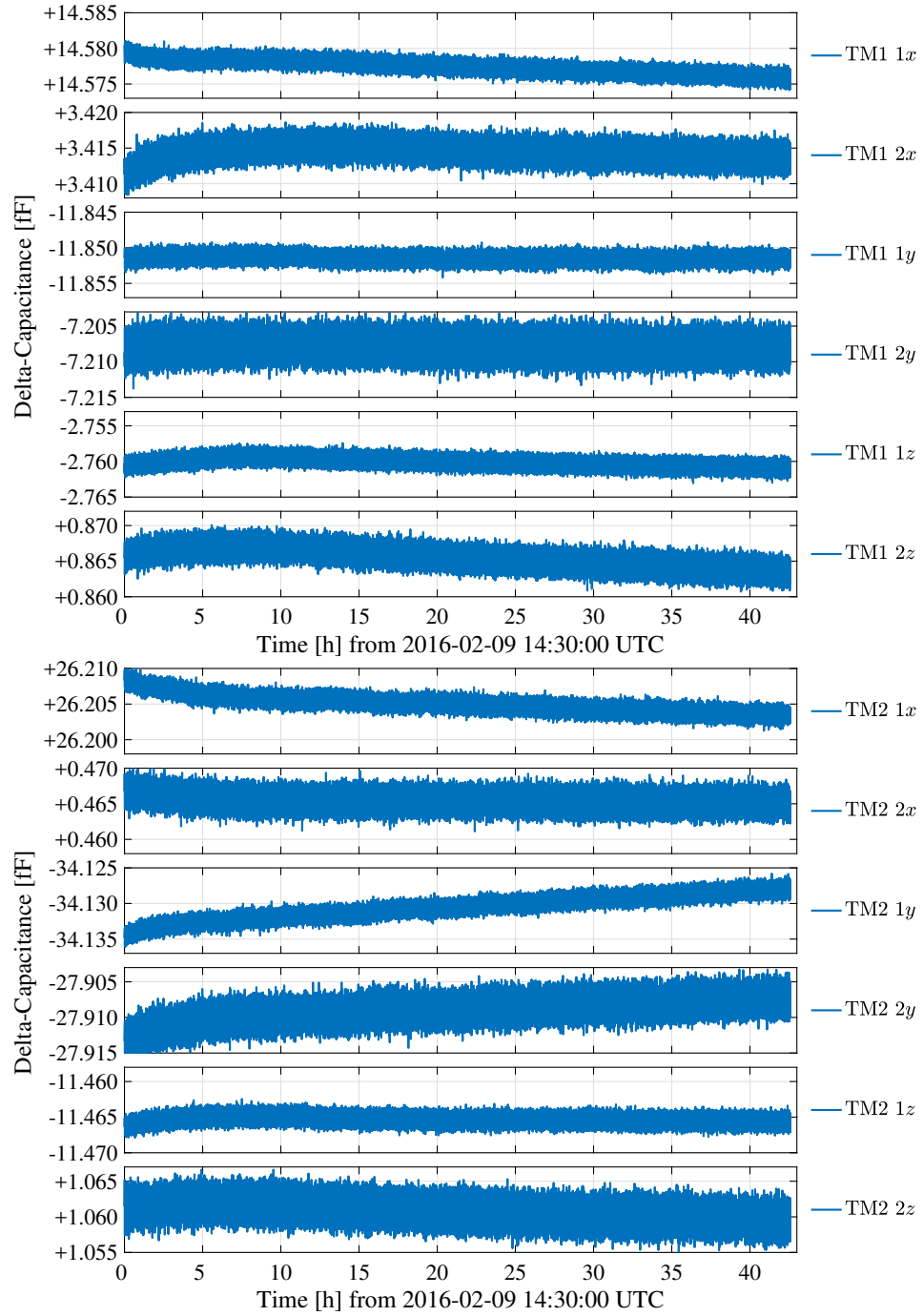
FIG. 4: TM1 and TM2 Time series for the different GRS sensing channels. Data have been acquired during LPF commissioning from February 9th, 2016 at 14:30 UTC until February 11th, 2016 9:05 UTC. Test Masses were grabbed by the plungers touching them on the z axis surfaces. Sampling frequency is 10 Hz. Despite the different absolute values, the y-ranges for the plots are spanning just 10 / 20 aF. We also observe the differences in the high frequency noise between $1x$, $1y$, $1z$ and $2x$, $2y$, $2z$ channels as already reported in section II.
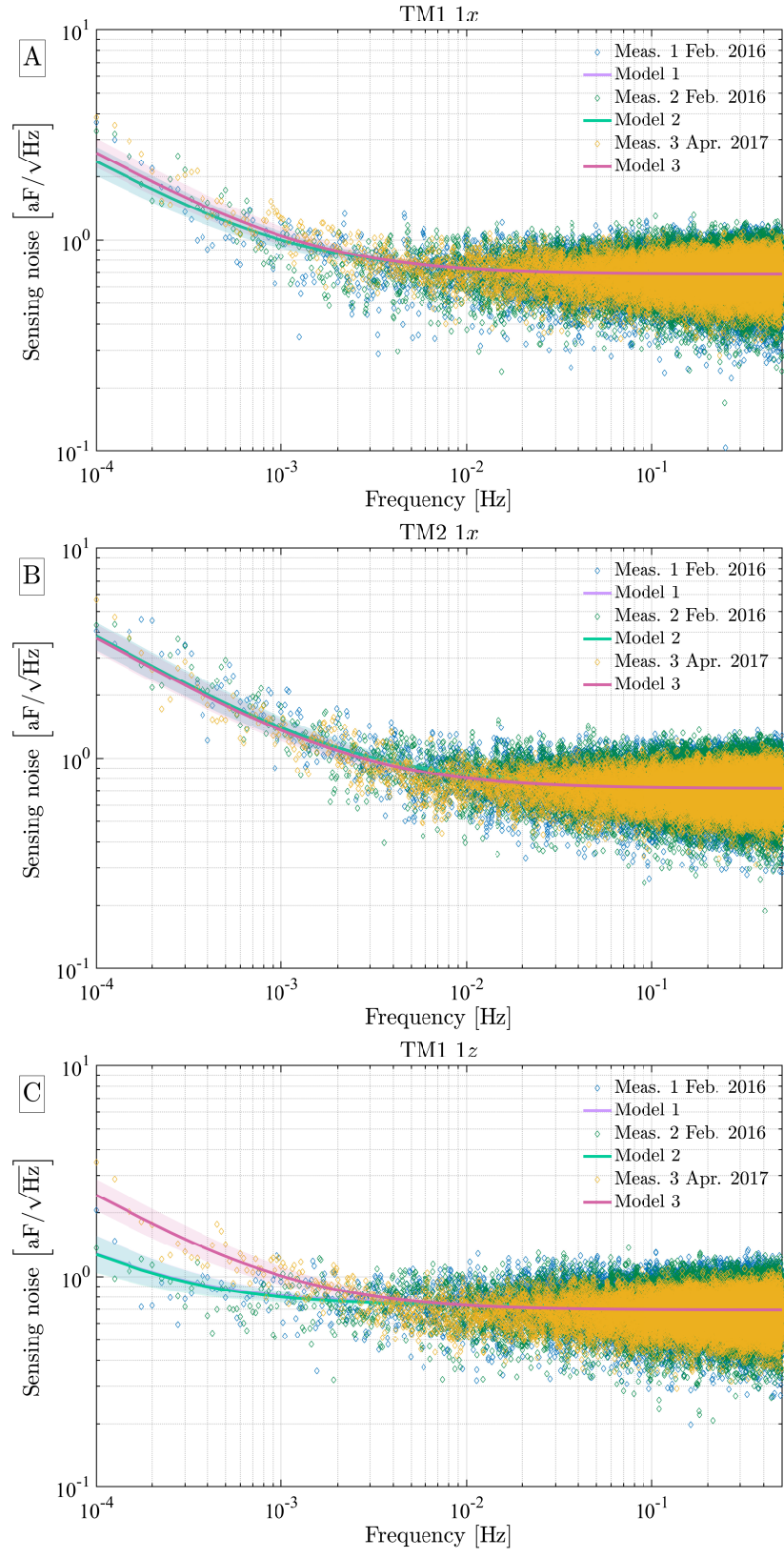
FIG. 5: Square root of the power spectral density of three selected channels, together with the corresponding models provided by equation (1) with the fit parameters reported in Tab. I. In all figures we report the three available datasets (two measured in Feb. 2016 and one measured in Apr. 2017). A) Measurements and models corresponding to channel TM1 $1x$. B) Measurements and models corresponding to channel TM2 $1x$. C) Measurements and models corresponding to channel TM1 $1z$. The difference observed between the measurements in Feb. 2016 and in Apr. 2017 is entirely due to the different position along z of the test mass during the two measurements. The average readout during Feb. 2016 was $-3.4\,\mathrm{fF}$, while during Apr. 2017 it was $-21.3\,\mathrm{fF}$. The increase of TM displacement corresponds to an enhancement of the effect of the position dependent noise (noise coefficient B).
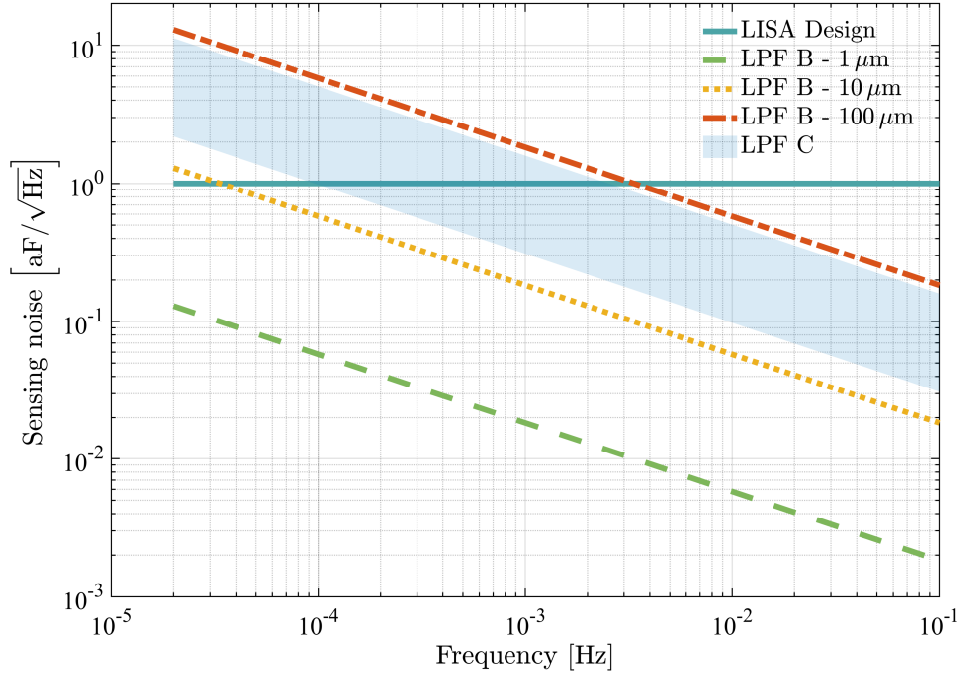
FIG. 6: Projection of the LPF GRS capacitive sensing noise within the extended LISA measurement band. The dark green line represents a possible design target for LISA. The dashed green, yellow and red lines are the contribution of B noise (position dependent, see equation 1) for a TM displacement of $1\,\mu$m, $10\,\mu$m and $100\,\mu$m respectively. The light blue shaded region represents the contribution from C noise (position independent, see equation 1). The lower and upper boundaries of the C noise area are set by the minimum and maximum values for C reported in Tab. I.

Tables

TABLE I: Table of B and C_j parameters for the noise model in equation (1). Parameters vales have been obtained as the average of the MCMC chains. Parameters errors corresponds to the standard deviation of the MCMC chains.

B (All channels) [ppm Hz$^{-1/2}$]	31 ± 2
C_j [aF Hz$^{-1/2}$]	
TM1 $1x$	0.57 ± 0.03
TM1 $2x$	0.54 ± 0.05
TM1 $1y$	0.85 ± 0.03
TM1 $2y$	0.49 ± 0.08
TM1 $1z$	0.31 ± 0.03
TM1 $2z$	0.64 ± 0.04
TM2 $1x$	0.87 ± 0.05
TM2 $2x$	1.10 ± 0.05
TM2 $1y$	0.40 ± 0.17
TM2 $2y$	1.59 ± 0.07
TM2 $1z$	0.43 ± 0.03
TM2 $2z$	1.12 ± 0.06